

International Journal of Structural Stability and Dynamics  
© World Scientific Publishing Company

## COMPARISON OF EIGENMODE BASED AND RANDOM FIELD BASED IMPERFECTION MODELING FOR THE STOCHASTIC BUCKLING ANALYSIS OF I-SECTION BEAM-COLUMNS

A. STAVREV, D. STEFANOV, D. SCHILLINGER and E. RANK

*Chair for Computation in Engineering,  
Department of Civil Engineering and Surveying,  
Technische Universität München,  
Arcisstr. 21, 80333 München, Germany  
{stavrev,stefanov}@mytum.de, {schillinger,rank}@bv.tum.de*

The uncertainty of geometric imperfections in a series of nominally equal I-beams leads to a variability of corresponding buckling loads. Its analysis requires a stochastic imperfection model, which can be derived either by the simple variation of the critical Eigenmode with a scalar random variable, or with the help of the more advanced theory of random fields. The present paper first provides a concise review of the two different modeling approaches, covering theoretical background, assumptions and calibration, and illustrates their integration into commercial finite element software to conduct stochastic buckling analyses with the Monte-Carlo method. The stochastic buckling behavior of an example beam is then simulated with both models, calibrated from corresponding imperfection measurements. The simulation results show that for different load cases, buckling load variabilities and corresponding mode shapes obtained from the Eigenmode based approach are in good accordance with those obtained from the random field based approach. This demonstrates that the simple variation of the critical Eigenmode is a valid basis for the stochastic analysis of imperfection sensitive I-section beam-columns.

*Keywords:* Finite element analysis; Stochastic buckling analysis; I-section beam-columns; Eigenmode based imperfection modeling; Random field based imperfection modeling.

### 1. Introduction

Due to their excellent properties under bending loads, thin-walled I-section beam-columns constitute one of the most frequently used construction elements in steel structures today. However, their open cross section made up of cantilevered thin plates causes a difficult failure process at ultimate strength, which usually combines both local plate buckling and global flexural-torsional buckling. In addition, I-section beam-columns are very sensitive to small changes in geometry, which drastically reduce their ultimate load bearing capacity compared to the resistance of the perfect member. The most common approach to take into account geometric imperfections in the analysis of I-section beam-columns is a deterministic model based on conservative worst case assumptions. It relies on the fact that thin-walled structures are particularly sensitive to imperfections in the shape of their Eigenmodes. The geometric deviation is therefore assumed to correspond to the critical

Eigenmode of the I-beam, which is expected to be triggered at ultimate strength. The deterministic Eigenmode based imperfection model is a suitable tool for the application in structural engineering practice with a focus on deriving reliable upper bounds to exclude buckling in worst case scenarios.

Due to the randomness of geometric imperfections, resulting from arbitrary influences during industrial manufacturing, transportation and on-site assembly, buckling loads of a series of nominally equal I-section beam-columns exhibit a large scattering. This uncertainty is an important aspect, for example when considering economic design or the probability of failure. Since experimental studies would involve buckling tests for very large numbers of I-sections, consuming prohibitively large financial and material resources, the analysis of the buckling load variability requires the application of modern simulation technology in conjunction with stochastic imperfection models. Over the last decade, several approaches have been reported in the literature, which can be generally classified into two categories: First, a simulation can be based on stochastic imperfection models, which extend the standard deterministic approach by a random variable. They can be handled reliably with basic knowledge of statistics, but involve the Eigenmode assumption. Second, a simulation can be based on random fields that represent the spatial variability of geometric imperfections. Random fields are thus capable of reproducing stochastic characteristics of experimental imperfection data without taking additional assumptions in terms of spatial shape or magnitude, but their application requires a deeper understanding of modern stochastic process theory. Their accuracy and reliability has been demonstrated in many computational studies for a range of thin-walled structures, such as beams, plates and shells.

In this context, the present paper intends to address the following key question: How closely do the results of the simple stochastic Eigenmode based model approximate the results of the random field based model, whose accuracy has been demonstrated in the literature? This question is of particular interest, since a close match of the results would underline that the simple Eigenmode model provides a valid basis for the stochastic simulation of I-section beam-columns. In the following, we give an answer by examining the example I-section beam, for which extensive measurements of geometric imperfections and experimental buckling test data for several nominally equal I-section members are provided by a data bank. Fig. 1 shows the examination process. First, a Gaussian random field based model is calibrated by deriving homogeneous and evolutionary power spectra from imperfection measurements. Using the spectral representation method, realizations of random imperfections are generated. Second, an Eigenmode based model is set up, which generates realization of imperfections with a single Gaussian random variable fitted to the measurements. Each stochastic imperfection model produces an arbitrary number of imperfect I-section beam samples, which can be analyzed with nonlinear finite elements (FE). In the sense of the Monte-Carlo method, the buckling load variability for each imperfection model is derived from the series of deterministic finite element results in terms of histograms and statistic key parameters.

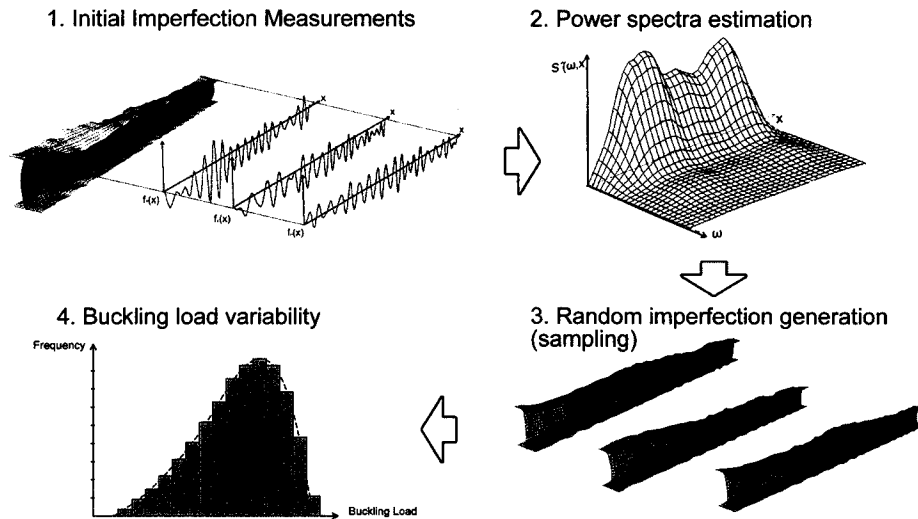


Figure 1: The four steps of the simulation with the random fields method.

The paper is organized as follows: Section 2 provides a brief review of relevant elements of the theory of random fields. Section 3 introduces the example I-section beam-column and discusses in detail the background, the assumptions and the calibration of a random field based and an Eigenmode based stochastic imperfection model. Section 4 briefly illustrates some aspects of the discretization and the non-linear analysis with the commercial FE software “MSC Nastran”. In section 5, the simulation results obtained with each imperfection model are presented and their stochastic characteristics are compared and assessed in detail. Section 6 summarizes the observations, concluding that the Eigenmode approach indeed constitutes a valid basis for the stochastic simulation of I-section beam-columns.

## 2. Some elements of the theory of random fields

The notion of a random field and its spectral representation are briefly reviewed, which are applied later on to set up a random field based model of geometric imperfections. Readers interested in a more detailed description are referred to <sup>?</sup>.

### 2.1. Random fields and their description

A random field, also known as a stochastic process, is an ensemble of functions that can be characterized stochastically. A Gaussian random field  $f(x)$  is completely characterized by a mean function  $\mu(x)$ , standard deviation  $\sigma(x)$  and an autocorrelation function. It is called homogeneous, if  $\mu(x)$ ,  $\sigma(x)$  and the autocorrelation

4 *A. Stavrev et. al.*

function do not change along  $x$ . If they do, we call the random field evolutionary. Considering the spectral representation of these parameters, we can estimate them from measurements as follows.

## 2.2. Power spectrum estimation

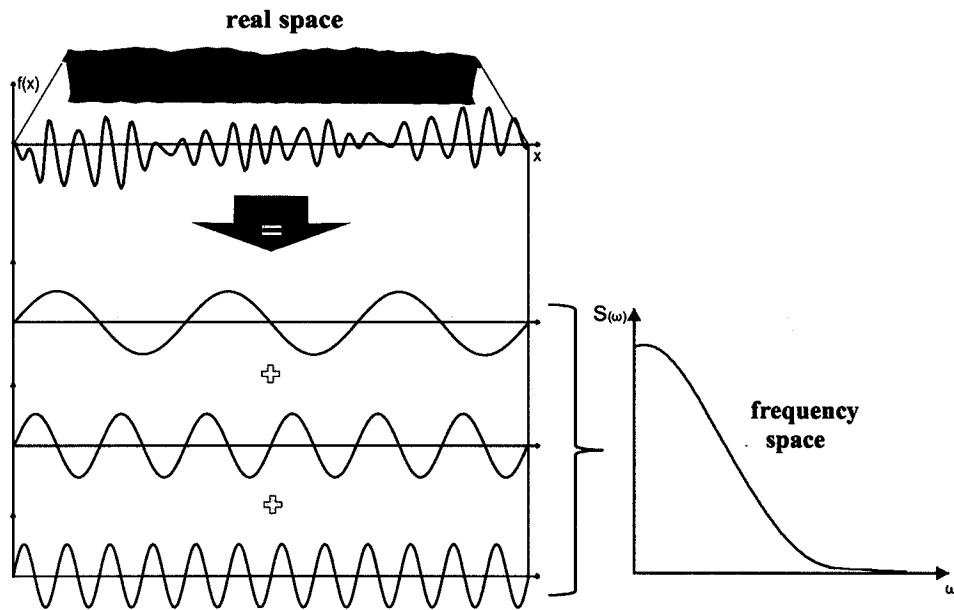


**Figure 2:** General power spectrum estimation using the Fourier transformation.

A random physical phenomenon can be described by a series of  $m$  measurements that are interpreted as realizations  $h^{(i)}(x)$ ,  $i = 1, 2, \dots, m$  of the underlying random field  $h(x)$ <sup>26,27,28,?</sup>. Measurements  $h^{(i)}(x)$  are first divided into a deterministic mean  $\mu(x)$  and zero-mean components  $f^{(i)}(x)$ . If the zero-mean field  $f(x)$  can be assumed to be homogeneous, the corresponding power spectrum  $S_h(\omega)$  can be estimated by the so-called periodogram<sup>25,45</sup> (see also Fig. 2.)

$$\tilde{S}_h(\omega) = E \left[ \frac{1}{2\pi L} \cdot \left| \int_0^L f^{(i)}(x) \cdot e^{-I\omega x} dx \right|^2 \right] \quad (2.1)$$

where the term in absolute value is the Fourier transform of  $f^{(i)}(x)$ ,  $E[\ ]$  denotes the operator of mathematical expectation,  $L$  is the length of  $f^{(i)}(x)$  and  $I$  is the complex unit. If the zero-mean part  $f^{(i)}(x)$  of the measurements are evolutionary and can be

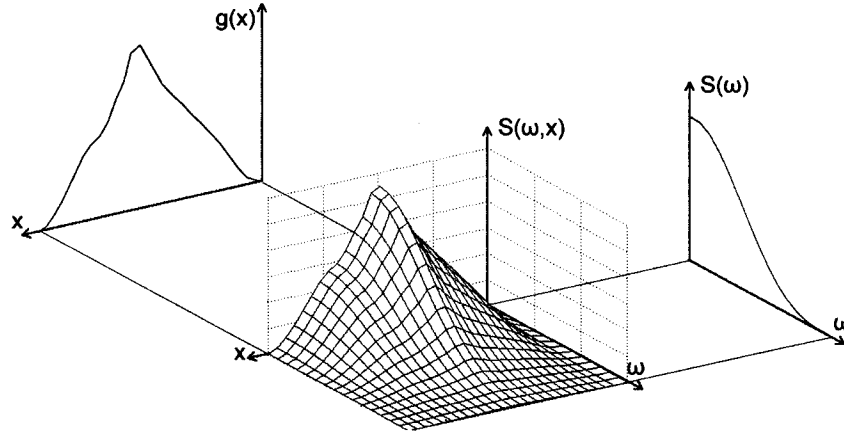


**Figure 3:** Example of an evolutionary power spectrum.

assumed to be approximately separable, the corresponding power spectrum  $S(\omega, x)$  (see Fig. 3.) can be estimated by the method of separation, recently introduced by SCHILLINGER and PAPADOPOULOS<sup>35</sup>

$$\tilde{S}(\omega, x) = E \left[ |f^{(i)}(x)|^2 \right] \cdot \frac{\tilde{S}_h(\omega)}{2 \int_0^\infty \tilde{S}_h(\omega) d\omega} \quad (2.2)$$

The left hand side of Eq. (2) denotes the estimated mean square; the right hand side represents a normalization of the periodogram based homogeneous estimate  $\tilde{S}_h(\omega)$  from Eq. (1). Due to the decoupling into a spatial and a frequency part, which simultaneously allows an accurate resolution in space and an optimum localization in frequency, the method of separation Eq. (2) is especially suitable for the robust estimation of strongly narrow-band power spectra, as they are typical for geometric imperfection measurements. The complete derivation of the method of separation and a comparison with standard techniques for the estimation of different benchmark spectra has been recently presented in<sup>35</sup>. In particular, this study shows both analytically and numerically that for separable spectra the estimation of Eq. (2) converges to the true spectrum for an infinite number of input samples. Furthermore, it shows that the method of separation yields considerably better estimation results for strongly narrow-band imperfection samples than any standard evolutionary estimation technique.

### 2.3. Spectral representation of a random field

If the power spectrum  $S_h(\omega, x)$  of  $f(x)$  is known, an arbitrary number  $m$  of corresponding random samples can be generated by the spectral representation method<sup>37,38,40</sup>, which reads for a one-dimensional univariate zero-mean Gaussian random

### 3. Stochastic imperfection modeling of an imperfect I-section beam-column

We consider the example of a typical I-section beam, for which measurements of geometric imperfections in a series of nominally equal beams are available from a data bank. We show in detail how to set up and calibrate corresponding random field based and Eigenmode based imperfection models.

#### 3.1. The example I-section beam-column

The report by Hasham and Rasmussen<sup>15</sup> contains extensive imperfection measurements and corresponding experimental buckling loads for a series of six nominally identical, 4 m long I-beams, whose nominal geometry is illustrated in Fig. 5.

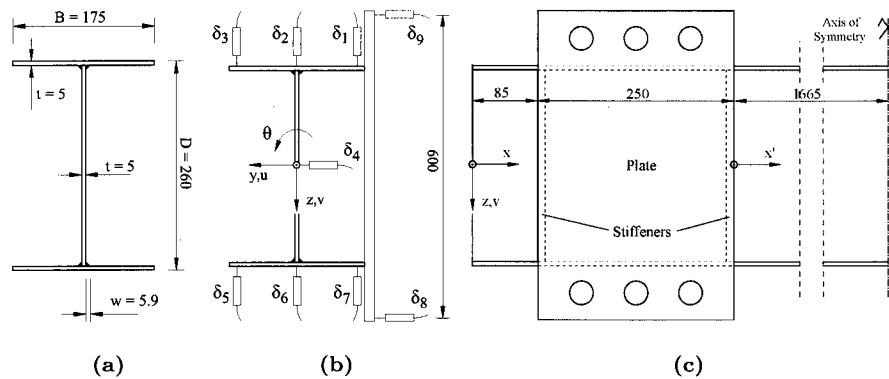


**Figure 5:** The I-section test member with total length of 4000 and free length of 3330 mm. **a** Cross-section dimensions. **b** Displacement transducers for imperfection measurement. **c** Length dimensions, additional stiffeners and plates.

The tested specimens were designed to be representative of doubly symmetric welded steel I-sections with typical levels of geometric imperfections, and were fabricated in the laboratory by the experimenters themselves. Web stiffeners and plates at the ends of the specimens enable levers to be rigidly connected for the transfer of moments. This reduces their free length to 3.33 m (see Fig. 5). The material is described by Young's modulus  $E = 2.1 \cdot 10^5 N/mm^2$  and Poisson's ratio  $\nu = 0.3$ , and the plate thickness  $t$  is 5 mm in both web and flanges. Since the focus of our study lies on the comparison of stochastic modeling approaches for geometric imperfections, all other parameters are assumed deterministic. For geometric imperfection measurements, displacement transducers were placed at nine cross-sectional locations  $\delta_1$  to  $\delta_9$  as shown in Fig. 5a. Under the assumption that the specimens are perfectly placed in the reaction frame as illustrated in Fig. 6., measurements were taken longitudinally at intervals of 25 mm referred to a straight line fitted between the two end points. The geometric imperfections are classified into local and global

6 *A. Stavrev et. al.*

field

$$f^{(i)}(x) = \sqrt{2} \sum_{n=0}^{N-1} A_n \cos(\omega_n x + \phi_n^{(i)}) \quad (2.3)$$

$$\text{with } A_n = \sqrt{2 \cdot S(\omega_n, x) \cdot \Delta\omega} \quad (2.4a)$$

$$\omega_n = n \cdot \Delta\omega \quad (2.4b)$$

$$\Delta\omega = \omega_{up}/N \quad (2.4c)$$

$$A_0 = 0 \vee S(\omega_0, x) = 0 \quad (2.4d)$$

where  $i = 1, 2, \dots, m$  and  $n = 0, 1, 2, \dots, (N - 1)$ . The parameter  $\omega_{up}$  is the cut-off frequency, beyond which the power spectrum is assumed to be zero, the integer  $N$  determines the discretization of the active frequency range, and  $\phi_n^{(i)}$  denotes the  $i^{th}$  realization of  $N$  independent phase angles uniformly distributed in the range  $[0, 2\pi]$  as shown in Fig. 4. To obtain samples of the original random field  $h(x)$ , the deterministic mean  $\mu(x)$  has to be superposed to Eq. (3).

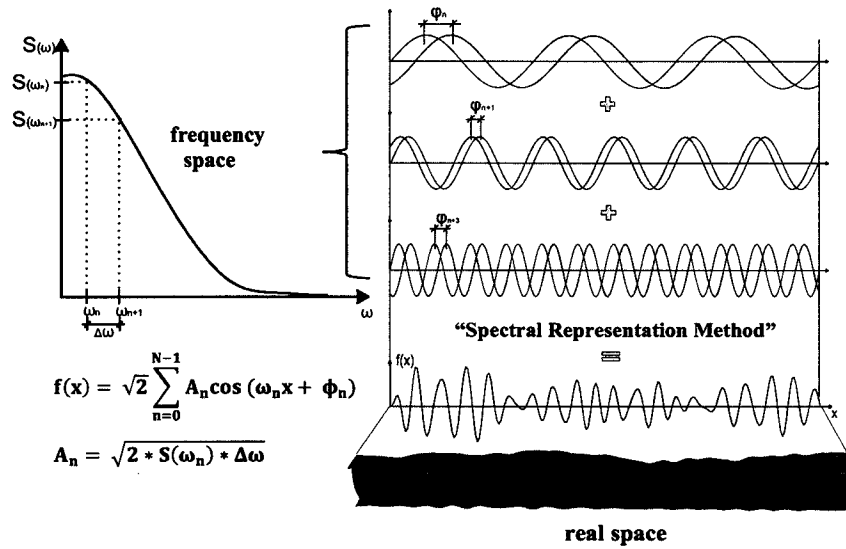
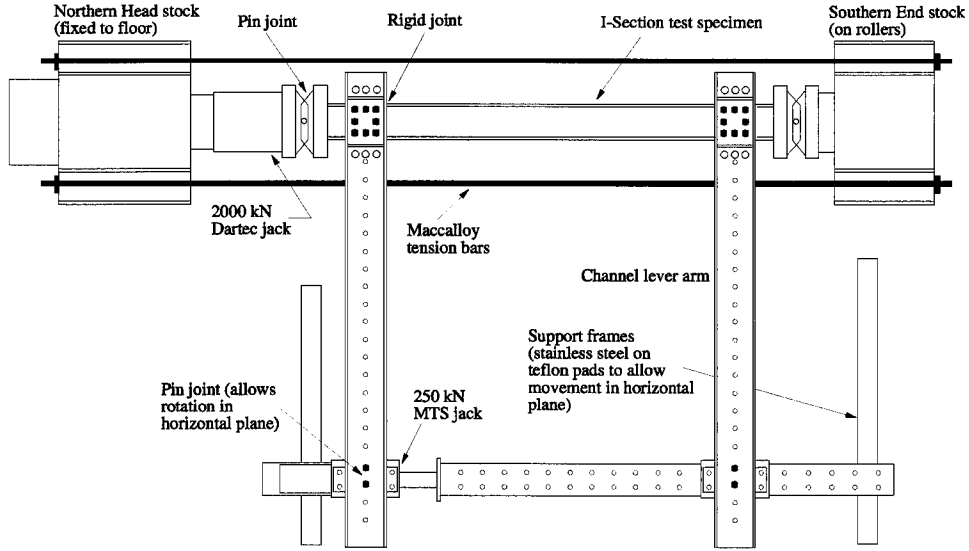


Figure 4: The spectral representation method.

8 *A. Stavrev et. al.*


**Figure 6:** Reaction frame for beam-column buckling tests.

imperfections. There are five types of local imperfections that were directly measured at positions  $\delta_1$ ,  $\delta_3$ ,  $\delta_4$ ,  $\delta_5$  and  $\delta_7$ . The three global imperfections  $u$ ,  $v$  and  $\theta$  were determined from the rest of the local measurements as follows:

$$u = \frac{\delta_8 + \delta_9}{2} \quad (3.1)$$

$$v = \frac{\delta_2 - \delta_6}{2} \quad (3.2)$$

$$\theta = \frac{\delta_9 - \delta_8}{600 \text{ mm}} \quad (3.3)$$

The parameters  $u$ ,  $v$  and  $\theta$  denote global cross-sectional deviations in weak and strong axis directions and rotation about the cross-sectional center of gravity. Some of the measurements are illustrated in Fig. 7.

### 3.2. Conceptual modeling of an imperfect I-beam

We follow the conceptual imperfection model derived by SCHILLINGER et al.<sup>36</sup> for a similar I-section, which fully accommodates all available measurements. The total geometric imperfection profile is assumed to be composed of five local components  $\lambda_1$  to  $\lambda_5$  and three global components  $\gamma_1$  to  $\gamma_3$  as illustrated in Fig. 8. Local imperfections denote local geometric deviations perpendicular to the flange and web plates in the cross-sectional plane. They are imposed onto the perfect outer flange

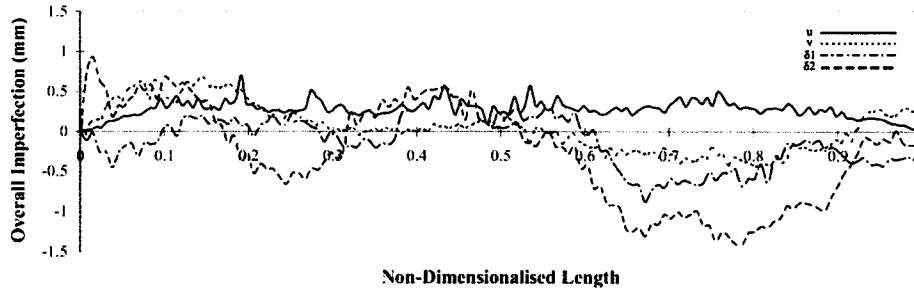


Figure 7: Example for geometric imperfection measurements.

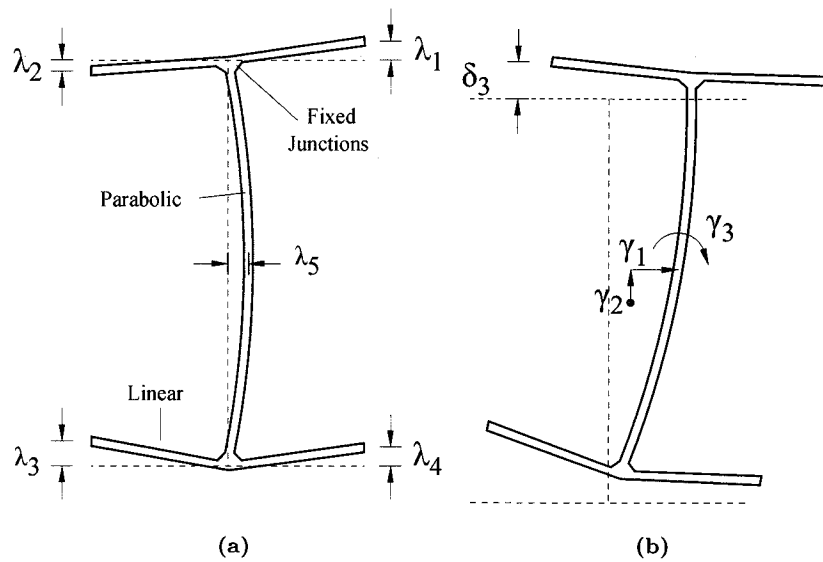


Figure 8: The eight different components of the total geometric imperfection. **a** Local imperfections  $\lambda$  at the flange edges and the web center. **b** Global imperfections  $\gamma$ .

edges and the web center, while the web-flange junctions remain perfect. Intermediate imperfections in flanges and web are interpolated linearly and parabolically, respectively. The assumptions of fixed junctions and interpolation shapes are confirmed by measurements at intermediate plate points in similar I-sections. Global imperfections  $\gamma_1$  to  $\gamma_3$  describe deviations from perfect alignment, i.e. weak and strong axis translations and cross-sectional rotation, which are superposed onto the locally imperfect geometry.

### 3.3. The random field based modeling approach

In the random field based model, local as well as global imperfections are assumed to be fully uncorrelated, and can thus be modeled by eight independent one-dimensional random fields along the longitudinal axis of the beam. Following SCHILLINGER et al. <sup>36</sup>, the five random field representations  $\lambda_k$ ,  $k = 1, \dots, 5$  for local components are assumed to be zero-mean and homogeneous, so that corresponding power spectra  $\tilde{S}_k(\omega)$  can be estimated by inserting measurements  $\delta_1$ ,  $\delta_3$ ,  $\delta_4$ ,  $\delta_5$  and  $\delta_7$  into the periodogram Eq. (1). The random field representation for global components  $\gamma_l$ ,  $l = 1, 2, 3$ , consist of mean functions  $\mu_l(x)$  evaluated from the corresponding series of processed measurements  $u$ ,  $v$  and  $\theta$ , and of the corresponding zero-mean evolutionary random fields, whose power spectra  $\tilde{S}_l(\omega, x)$  are estimated by inserting the zero-mean parts of  $u$ ,  $v$  and  $\theta$ , into the method of separation Eq. (2). In view of Eq. (3), an arbitrary number of local and global random field samples  $\lambda_k$  and  $\gamma_l$  can then be generated by spectral representation as

$$\lambda_k^{(i)}(x) = \sqrt{2} \sum_{n=0}^{N-1} A_{k,n} \cdot \cos(\omega_n x + \phi_n^{(i)}) \quad (3.4a)$$

$$A_{k,n} = \sqrt{2 \cdot \tilde{S}_k(\omega_n) \cdot \Delta\omega} \quad (3.4b)$$

$$\gamma_l^{(i)}(x) = \mu_l(x) + \sqrt{2} \sum_{n=0}^{N-1} A_{l,n} \cdot \cos(\omega_n x + \phi_n^{(i)}) \quad (3.5a)$$

$$A_{l,n} = \sqrt{2 \cdot \tilde{S}_l(\omega_n, x) \cdot \Delta\omega} \quad (3.5b)$$

where  $\Delta\omega = 3 \cdot 10^4$  rad/mm and parameters  $i$ ,  $n$  and  $\phi$  are defined in Eq. (3).

Despite the analogy between the experimental measurements and the imperfection model, the power spectra directly obtained from experimental data are inaccurate, because imperfection measurements comprise both local and global components. This is illustrated in Fig. 5 by comparing the measured flange imperfection  $\lambda_3$  with its purely local counterpart  $\lambda_2$  of the conceptual model, which are completely different. We follow the solution proposed by SCHILLINGER et al. <sup>36</sup>, who separate the imperfection measurements in the frequency domain  $\omega$  into two distinct parts that contain smaller local wave-lengths and larger global wave-lengths, respectively. Since imperfections in the form of Eigenmodes of the perfect structure have potentially the most decisive influence <sup>4,6,14,45</sup>, it is sufficient to separate the critical local and global wave-lengths that correspond to a local or global buckling mode of the perfect I-section member.

The global buckling modes of the perfect beam correspond to Euler modes that include at most two half-waves in longitudinal direction, whereas the lowest local buckling mode consists of several half-waves (see for example Fig. 11.). Hence the

frequency domain is partitioned into two distinct frequency parts

$$\omega_{global} = (0.0000 ; 0.0024) \text{ [rad/mm]} \quad (3.6a)$$

$$\omega_{local} = (0.0024 ; 0.0150) \text{ [rad/mm]} \quad (3.6b)$$

The transition point corresponds to 2.5 half-waves, so that long-wave components around the relevant Euler modes are attributed to the global imperfections and short-wave components around the relevant local buckling modes are attributed to the local imperfections. Frequencies beyond the upper cut-off frequency of  $\omega = 0.015 \text{ rad/mm}$  are not taken into account. Fig. 9. shows examples of a homogeneous spectrum for local imperfections, an evolutionary spectrum for global imperfections, and the corresponding mean function, all estimated from six measurements. Evolutionary power spectra are released from spurious high-frequency oscillations in spatial direction, which are a consequence of the small number of input measurements, with the spectral smoothing procedure suggested by SCHILLINGER and PAPADOPOULOS<sup>35</sup>.

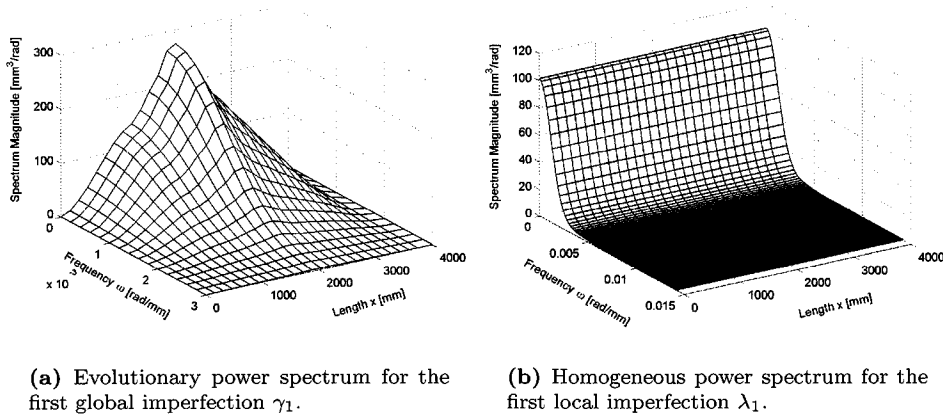


Figure 9: Examples of evolutionary and homogeneous power spectra.

The complete geometric profile at each longitudinal position  $x$  is obtained by mapping the initial perfect cross-sectional geometry  $(y, z)$  to the imperfect cross-sectional geometry  $(Y, Z)$  in the form

$$\begin{bmatrix} Y \\ Z \end{bmatrix} = \begin{bmatrix} y \\ z \end{bmatrix} + \underbrace{\left( \begin{bmatrix} 0 \\ \lambda_k \frac{2y}{B} \end{bmatrix} + \begin{bmatrix} \lambda_5 \left( \frac{1-z^2}{(D-t)^2} \right) \\ 0 \end{bmatrix} \right)}_{\text{local components}} + \underbrace{\begin{bmatrix} \gamma_1 \\ \gamma_2 \end{bmatrix} + \begin{bmatrix} \cos\gamma_3 & -\sin\gamma_3 \\ \sin\gamma_3 & \cos\gamma_3 \end{bmatrix} \cdot \begin{bmatrix} y \\ z \end{bmatrix}}_{\text{global components}} \quad (3.7)$$

where  $B$ ,  $D$  and  $t$  denote flange width, section height and plate thickness of the I-section according to Fig. 5. The flange index in  $\lambda_k$ ,  $k = 1 \dots 4$  has to be chosen

12 *A. Stavrev et. al.*

according to the current flange position of  $(y, z)$ . Imperfection samples generated from the random field based model are illustrated in Fig. 10, consisting of local homogeneous flange and web imperfections, global non-homogeneous translations and cross-sectional rotation.

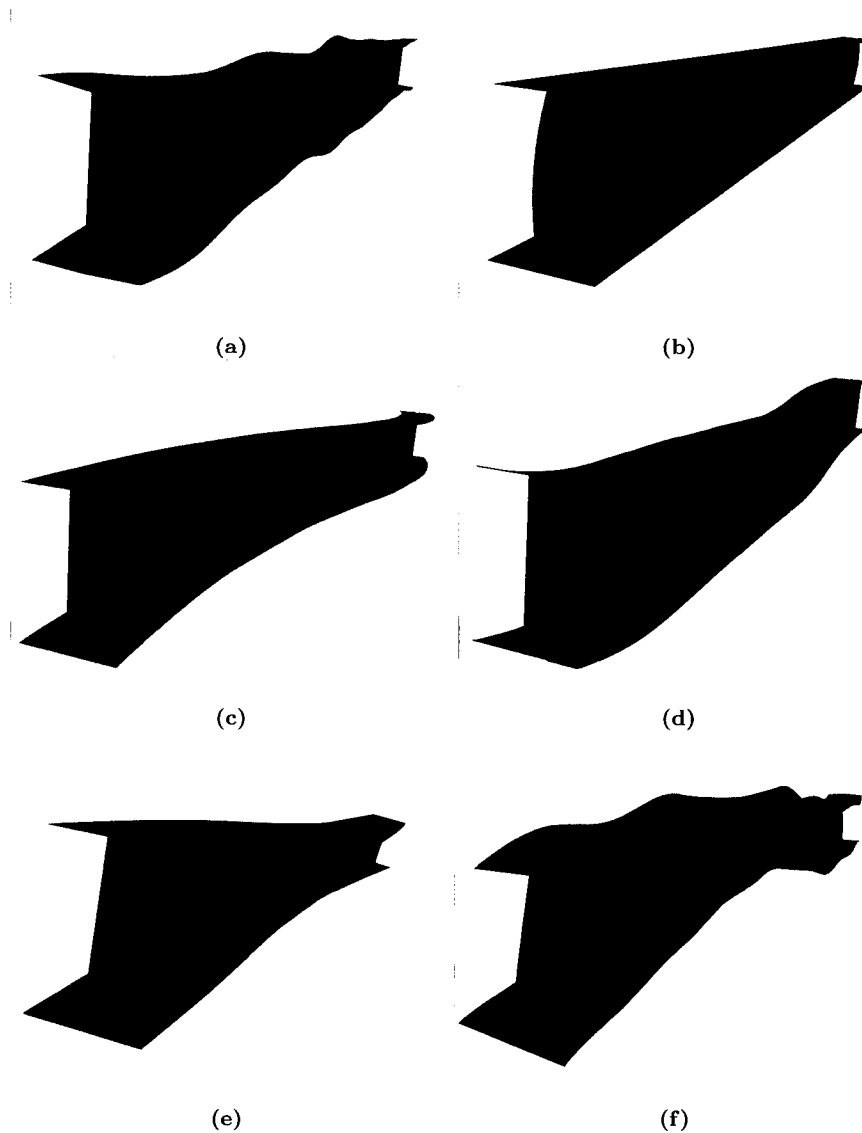


**Figure 10:** I-section sample with local and global geometric imperfections by the random field approach (magnified by 100). **a** Flange imperfection  $\lambda_1 - \lambda_4$ . **b** Web Imperfection  $\lambda_5$ . **c** Weak axis translation  $\gamma_1$ . **d** Strong axis translation  $\gamma_2$ . **e** Cross-sectional Rotation  $\gamma_3$ . **f** Complete Imperfection Eq. (3.7)

### 3.4. The Eigenmode based modeling approach

The Eigenmode based approach for the stochastic modeling of geometric imperfections can be regarded as a simple extension of the standard deterministic concept, which is an integral part of modern design codes and regulations. For the current example of an I-section beam-column, design standards define the critical global Eigenmode as a half sine wave, so that global imperfection samples  $\gamma_l$  read

$$\gamma_l(x) = A_{glob,l} \cdot \sin\left(x \frac{\pi}{L_0}\right) \quad (3.8)$$

where the scalar  $A_{glob,l}$  denotes the amplitude at mid-span,  $l = 1, 2, 3$  is a counter denoting again weak and strong axis translations and rotations, respectively, and  $L_0$  is the free length of the beam. The critical local Eigenmode is assumed here in the form of the lowest local Eigenmode of the perfect structure, which can be determined for example by a FE based linear buckling analysis for the load case under consideration. As an example, Fig. 11. illustrates the lowest local Eigenmode of the perfect I-section beam-column under pure compression. A scalar local imperfection

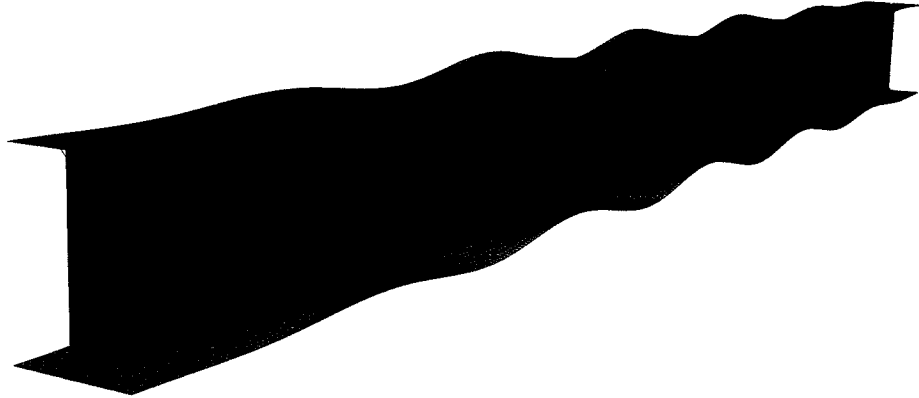


**Figure 11:** Failure mode of the perfect I-section obtained by linear buckling analysis with MSC NASTRAN. Displacements magnified by 80 for the visualization.

field  $f_{loc}(x, y, z)$  is obtained by deducting the perfect geometry from the local mode shape and normalizing the result with respect to its largest absolute value. In analogy with Eq. (3.8), it can be used to derive a deterministic local imperfection model in the form

$$\lambda(x, y, z) = A_{loc} \cdot f_{loc}(x, y, z) \quad (3.9)$$

which can be modulated by a suitable scalar amplitude  $A_{loc}$ .

The introduction of uncertainty in the Eigenmode based global and local imperfection models of Eqs. (3.8) and (3.9) can be simply achieved by considering the

scalar amplitudes  $A_{glob,l}$  and  $A_{loc}$  as Gaussian random variables

$$A_{glob,l} = \mu_{glob,l} + \sigma_{glob,l} \cdot Z \quad (3.10a)$$

$$A_{loc} = \sigma_{loc} \cdot Z \quad (3.10b)$$

where  $\mu_{glob,l}$  and  $\sigma_{glob,l}$  with  $l = 1, 2, 3$  denote the means and standard deviations of the global weak and strong axis translations and the global rotation, respectively, and  $\sigma_{loc}$  is the standard deviation of the local imperfection profile. Parameter  $Z$  denotes a zero-mean random variable with the standard Gaussian probability distribution. The free parameters of the simplified Eigenmode based imperfection model are the mean and standard deviations of Eqs. (3.10a) and (3.10b), for which a variety of calibration approaches could be thought of, accommodating the preference of the design engineer or the safety requirements of the project. For example, a very conservative calibration could determine  $\mu_{glob,l}$  from the maximum values that occur in the global measurements  $u$ ,  $v$ , and  $\theta$  of Eqs. (3.1) through (3.3).

In the present case, we are interested in a calibration, which accommodates most of the ideas of the random field based model, so that the comparability of the random field based and the Eigenmode based models is not biased by different assumptions. Therefore, we calibrate the parameters of the Eigenmode based model by using the information of the random field based model in the following way:

- In analogy with the previous section, we assume in Eq. (3.) a non-zero-mean distribution of the amplitude  $A_{loc}$  for global imperfections and in Eq. (3.) a zero-mean distribution of the amplitude  $A_{loc}$  for local imperfections.
- For the global translations and rotation, the means  $\mu_{glob,l}$  are the values of the mean functions  $\mu_{glob,l}(x = L_0/2)$  of Section 3.3 at mid-span.
- Using the fact that the standard deviations can be obtained from an integration of the spectrum over the frequency range  $\omega$ , the global standard deviations  $\sigma_{glob,l}$  can be determined from corresponding estimated evolutionary power spectra  $\tilde{S}_{glob,l}(\omega, x = L_0/2)$  of Section 3.3 at mid-span

$$\sigma_{glob,l}^2 = 2 \int_{0.0000}^{0.0024} \tilde{S}_{glob,l}(\omega, x = L_0/2) d\omega \quad (3.11)$$

where the integral takes into account the frequency range of Eq. (3.).

- Using the same identity, the standard deviation  $\sigma_{loc,l}$  of the local imperfection profile is chosen as the maximum of the five integrals of the estimated homogeneous power spectra  $\tilde{S}_{loc,k}(\omega, x = L_0/2)$  of Section 3.3

$$\sigma_{loc}^2 = \max_k \left( \int_{0.0024}^{0.0150} \tilde{S}_{loc,k}(\omega) d\omega \right) \quad (3.12)$$

where the integrals take into account the frequency range of Eq. (3.). The choice of the maximum in Eq. (3.) accommodates the conservative character of the Eigenmode based approach.

Assuming that all global and local imperfections are uncorrelated, independent random samples for the translation in the weak axis  $\gamma_1(x)$ , the translation in the strong axis  $\gamma_2(x)$ , the cross-sectional rotation  $\gamma_3(x)$  and the local imperfection profile  $\lambda$ . With respect to the random field based model of the previous section, the local imperfection field  $f_{loc}(x, y, z)$  can be interpreted as being composed of fully correlated single local flange and web imperfections, which again underlines the conservative character of the Eigenmode based model. The complete geometric imperfection profile  $(Y, Z)$  of the I-section at longitudinal position  $x$  is obtained again by mapping the imperfections onto the perfect geometry  $(y, z)$  as follows

$$\begin{bmatrix} Y \\ Z \end{bmatrix} = \begin{bmatrix} y \\ z \end{bmatrix} + \left( \lambda + \begin{bmatrix} \gamma_1 \\ \gamma_2 \end{bmatrix} + \begin{bmatrix} \cos\gamma_3 & -\sin\gamma_3 \\ \sin\gamma_3 & \cos\gamma_3 \end{bmatrix} \cdot \begin{bmatrix} y \\ z \end{bmatrix} \right) \quad (3.13)$$

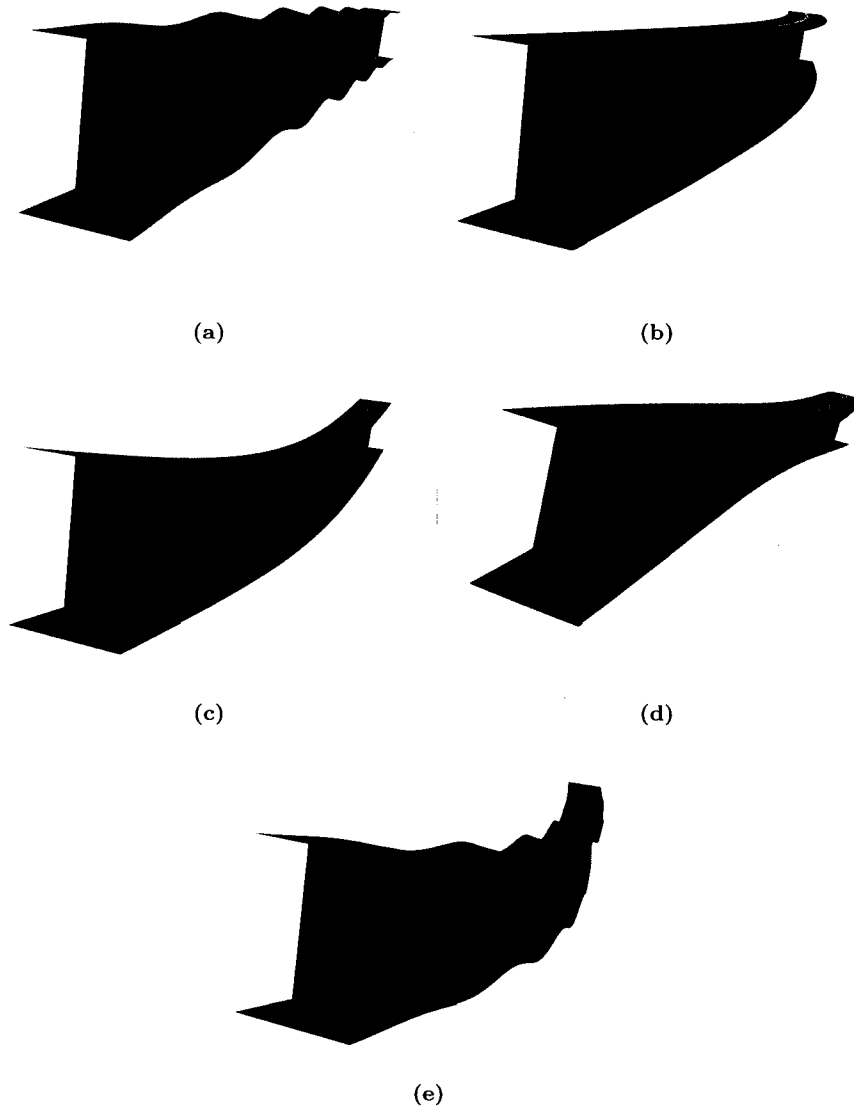
Fig. 12. illustrates the local and global components and the complete imperfection profile of an Eigenmode based I-section sample.

#### 4. Stochastic buckling analysis using a commercial FE program

To illustrate that buckling load variabilities can be determined without the availability of specialized software or an expert knowledge in advanced stochastic methods, we integrate our geometric imperfection models into a generally available commercial FE solver and the Monte-Carlo method. We provide details on the discretization of an I-section sample and the geometrically nonlinear analysis of the buckling load.

##### 4.1. Finite element discretization of an I-section beam-column

All finite element computations are performed with the commercial FE program "MSC Nastran". We discretize the beam geometry with quadrilateral elements of type "CQUAD4", which are standard 4-noded bilinear shell elements, taking into account membrane and bending as well as transverse shear (thick shell theory). Random field based and Eigenmode based imperfections can be simply incorporated into the finite element discretization by adjusting the nodal positions according to the imperfect geometry prescribed by Eqs. (3.7) and (3.13), respectively. A corresponding discretization of the I-section beam is shown in Fig. 13. The finite element discretization takes into account only the free-length part of the I-section beam samples in the reaction frame of Fig. 6. The interface between the free length part and the stiffened ends (see Fig. 13a) are described by appropriate displacement boundary conditions. Due to the perfect pins at the member ends, rotations about the major  $y$ -axis and translations along the  $x$ -axis are left unconstrained. According to <sup>15</sup>, rotations about the minor  $z$ -axis are constrained. Due to additional stiffeners and plates, rotations about the longitudinal axis and translations along the  $y$ -axis are prevented. The central web points at both boundaries are constrained against  $z$ -axis translations, and the central web point at one boundary against  $x$ -axis translation. The additional axial stiffness and moments of inertia due to the welds at the

16 *A. Stavrev et. al.*

**Figure 12:** I-section sample with local and global geometric imperfections by the eigenmode based approach (magnified by 100). **a** Complete local imperfection  $\lambda_1 - \lambda_5$ . **b** Weak axis translation  $\gamma_1$ . **c** Strong axis translation  $\gamma_2$ . **d** Cross-sectional Rotation  $\gamma_3$ . **e** Complete Imperfection Eq. (3.16)

flange-web junctions are compensated by slightly increasing the thicknesses of shell elements as illustrated in Fig. 13b. Experiments show that web-flange junctions remain unaffected by local buckling deformations<sup>15</sup>. Following SCHILLINGER et al.<sup>36</sup>, this is ensured by a triangle of three very stiff truss elements that connect the

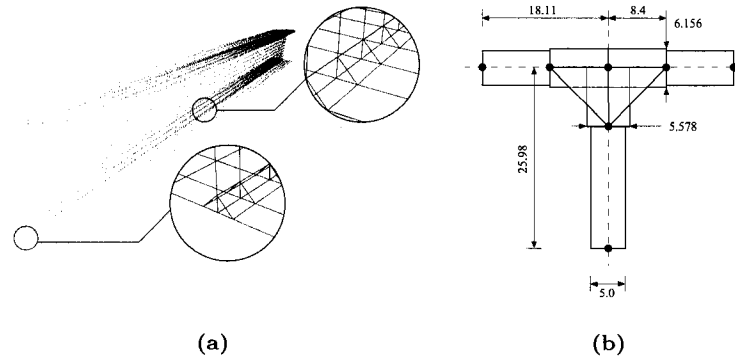


**Figure 13:** Finite Element Model of the Free-Length member. **a** Discretization of a perfect beam-column with quadrilateral shell elements. **b** Model of the flange-web junctions including thicker shell elements and additional truss elements.

outer junction nodes (see Figs. 13a and 13b) and prevent a relative deformation within the junction. Note that triangles of truss elements do not introduce spurious bending stiffness and do not interact with each other along the longitudinal axis. Since the support conditions in the reaction frame prevent out-of-plane distortion of the cross-section, corresponding warping constraints are imposed by small beam elements at both ends of the I-section member. Their stiffness components required to constrain out-of-plane distortion, i.e. bending stiffness around the global  $z$ -axis in the flanges and torsional stiffness in the web, is very large, while all other stiffness components are reduced to very small values.

#### 4.2. Finite element based buckling analysis

At both beam ends, force boundary conditions resulting from the compression and bending jacks of the reaction frame are transferred to equivalent stresses in  $x$ -direction. Furthermore, the effect of the weight of the I-section member and half of the moment actuator bracings and levers is considered by applying equivalent displacements in  $y$ -direction, calculated beforehand according to Euler-Bernoulli beam theory. The buckling load of a geometrically imperfect I-beam sample is determined by a geometrically nonlinear FE analysis, which takes into account large deformation effects. The arc-length procedure is applied to track the equilibrium path, which simultaneously increases all applied forces, until a bifurcation or limit point is found, associated with buckling failure. The constitutive law is isotropic elasticity. Thus, we assume that the failure of the beam occurs at a deformation state, which is purely elastic, and no plasticity and residual stress effects are taken into account during the simulation. For a more involved computational model that takes into account plasticity and residual stresses as well as random field based thickness and geometric imperfections at the same time, see SCHILLINGER et al.<sup>36</sup>. A suitable mesh density for imperfect I-section beam columns is determined by

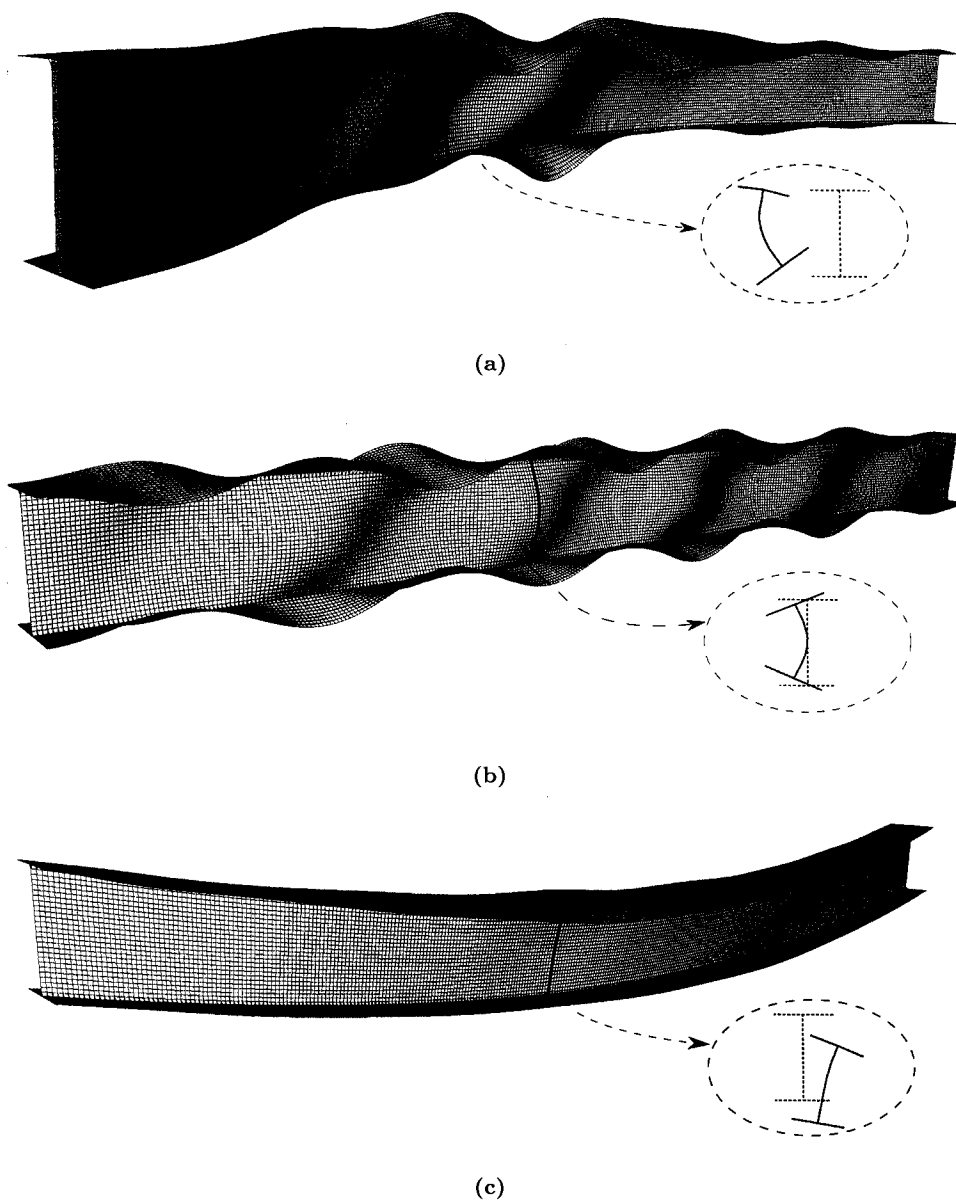


**Figure 14:** Various failure modes of beam samples computed by the Monte-Carlo random field based simulation . **a** Lateral torsional buckling. **b** Pure local flange and web buckling. **c** Lateral torsional buckling, loads case  $M/P = 0.050$ .

just a global translation along the weak axis or global rotation around the I-section center, respectively. A very rare mode is pure local flange and web buckling, which occurred only once in an almost perfect I-section beam-column. Under compression

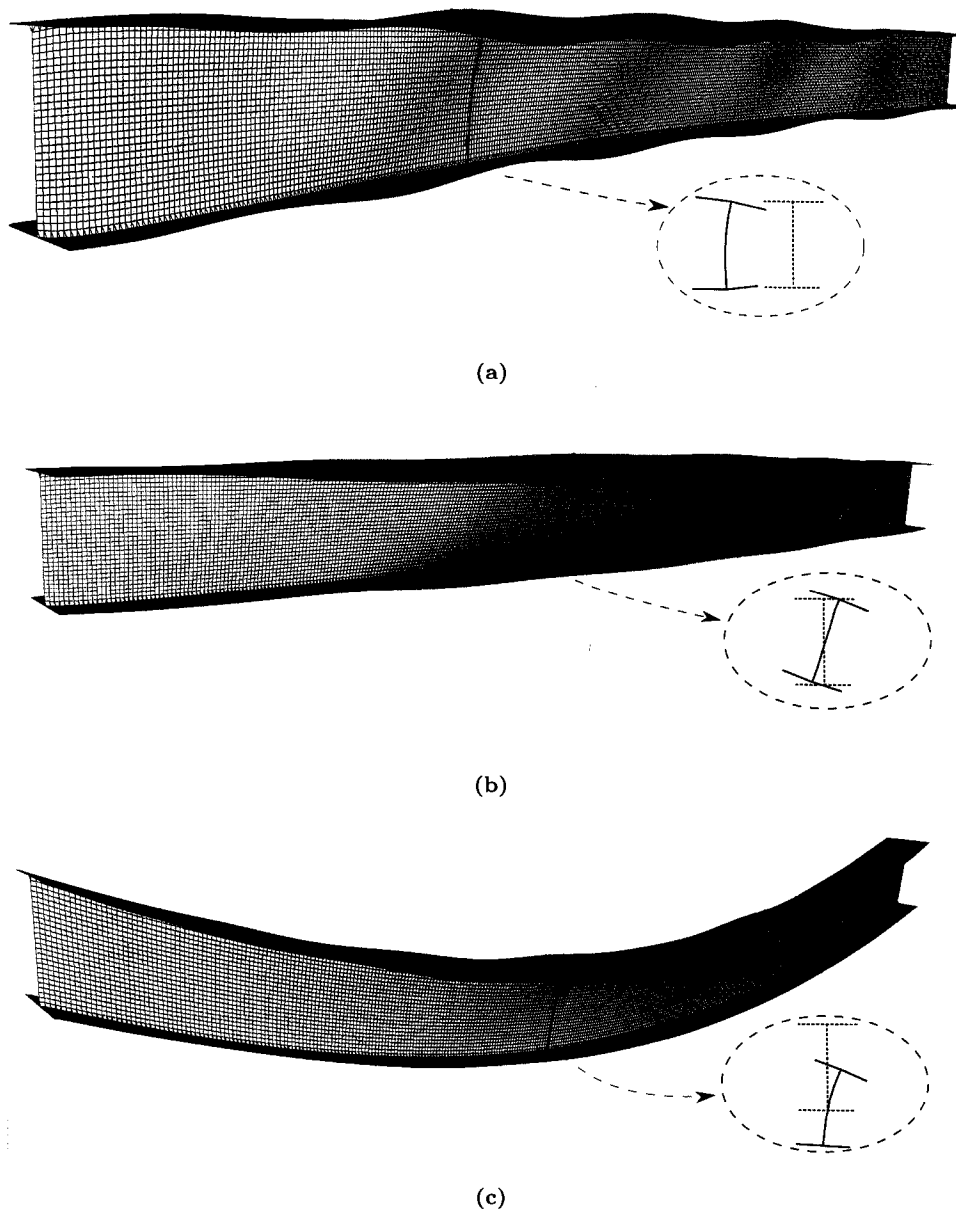


**Figure 15:** Various failure modes of beam samples computed by the Monte-Carlo Eigenmode based simulation. **a** Lateral torsional buckling. **b** Torsional buckling. **c** lateral torsional buckling with dominant flexural buckling for pure major axis bending.

dominated loads, one flange is in tension and therefore stabilized. The most frequent failure mode in this case consists of combined local plate buckling in the flange under

compression and a global rotation of the compressed part of the I-section.

These observations show that both geometric imperfection models are able to trigger a range of different failure modes. The dominance of global flexural-torsional buckling is in accordance with engineering experience for this kind and length of I-beams and corresponds well with the observations reported in <sup>4,43,?</sup>. For shorter I-beams of the same cross-section, only local failure modes occur <sup>36</sup>.

### 5.2. Buckling load variability of the random field based approach

The buckling load variabilities of all six load cases obtained with the random field based imperfection model are shown in the histograms of Figs. 16 through 21, which can be regarded as an approximation of the probability distribution of the buckling load. For the load case of pure compression, the decrease in ultimate strength with respect to the first bifurcation point of the perfect structure amounts to more than 30% and more than 45% compared to the mean and the lowest encountered buckling load, respectively, while for pure bending, the same comparison yields a decrease of ... % and ... %. Thus, the random field based imperfection model is able to simulate the considerable influence of geometric imperfections on the ultimate strength of thin-walled I-sections. The coefficient of variation  $Cov$  represents a normalized measure of stochastic dispersion independent of the absolute value of the buckling load, which thus allows an objective comparison of the buckling load variability of the present I-beam with those of the shorter I-beam of the same cross-section and a thin cylindrical shell, all examined under pure compression. The current 3.33 m long I-section beam-column exhibits a  $Cov$  of 6.6%, which is significantly higher than the  $Cov = 1.3%$  observed in the 1.33 m long beam-column of the same cross-section <sup>36</sup>. This demonstrates the dramatic increase of the buckling load variability with the length of the I-beam. The coefficient of variation of the buckling load under pure compression is thus almost comparable to the scattering of the buckling load in a cylindrical shell ( $Cov = 8%$ ), which is another classical example of an imperfection sensitive structure. With increasing moment, the mean value of the maximum normal force decreases constantly from  $\mu = 691.03kN$  under pure compression to  $\mu = 139.1kN$  under a force moment ratio of  $M/P = 0.5$  m. In addition, for bending dominated load cases, the scattering of buckling loads dramatically increases to coefficients of variations up to  $Cov = 30%$  in Fig. 20.

Comparing the histograms of the different load cases, we can observe that under axial load only, the probability distribution is symmetric and similar to a normal distribution. However, with increasing bending moment, the probability distribution of the buckling load becomes skewed, so that the bulk of the values lie to the left of the mean and a tail on the right side occurs, and thus resembles more a log-normal distribution. This is also confirmed by the positive skewness  $\gamma > 0$ , which provides an objective measure of the asymmetry of the probability distribution.

22 A. Stavrev et. al.

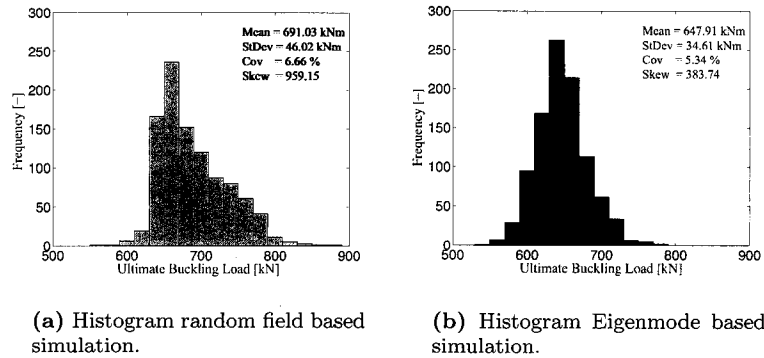


**Figure 16:** Buckling loads distributions of I-section members for the load case pure compression P.

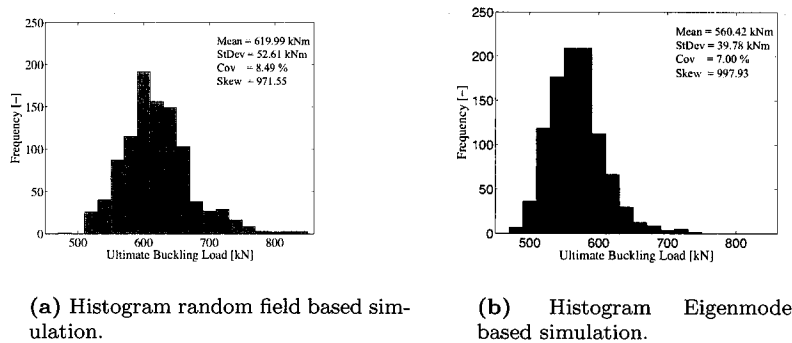


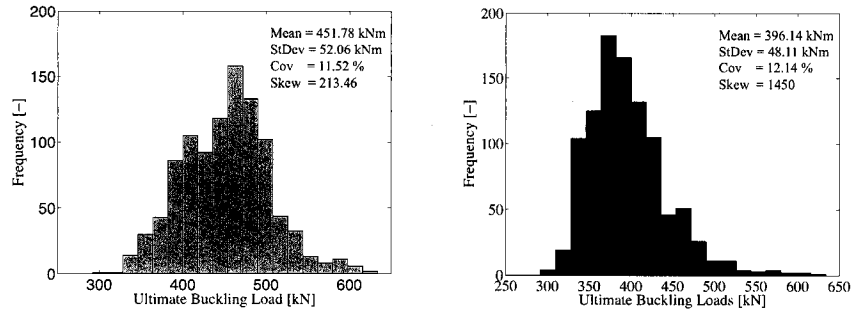
**Figure 17:** Buckling loads distributions of I-section members for the load case  $M/P = 0.050$ .

### 5.3. Buckling load variability of the Eigenmode based approach

In analogy with the previous sub-section, Monte-Carlo simulations are conducted with random Eigenmode based geometric imperfections. The resulting buckling load variabilities are displayed in Figs. 16 through 21, side by side with the corresponding random field based results. A first visual comparison of the histograms indicates that the two different imperfection models lead to very similar results. The form of the probability distribution follows the same trend, changing its shape with increasing moment from an approximately normal distribution to a skew distribution with a tail on the right. With respect to the minimum and maximum buckling loads, both imperfection models are in surprisingly good accordance throughout all load cases.

Taking a more detailed look at the stochastic key parameters, we can observe further similarities. The increase in skewness  $\gamma$  confirms the changing shape of the distribution. Furthermore, the surge in scattering with increasing end moments is

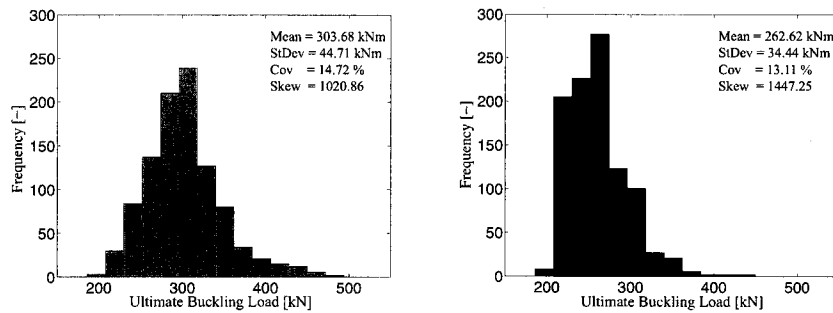
Comparison of Eigenmode based and random field based imperfection modeling 23



(a) Histogram random field based simulation.

(b) Histogram Eigenmode based simulation.

Figure 18: Buckling loads distributions of I-section members for the load case  $M/P = 0.125$ .



(a) Histogram random field based simulation.

(b) Histogram Eigenmode based simulation.

Figure 19: Buckling loads distributions of I-section members for the load case  $M/P = 0.250$ .

reproduced, which is illustrated by an increase in the corresponding coefficients of variation from  $Cov = 5.3\%$  to a maximum of around  $Cov = 40\%$ . With increasing moment, the mean value of the maximum normal force decreases constantly within the same range. However, the Eigenmode based imperfection model leads in general to lower means throughout all load cases and to much higher standard deviations and coefficients of variation for the dangerous bending dominated load cases, which underlines its conservative character. A tentative explanation for this characteristic behavior of the probability distributions is the comparability of the imperfections in terms of amplitudes, since both models are calibrated from the same power spectra, but the missing comparability in terms of frequencies. While the random field based model randomly contains all frequencies contained in the power spectra, the Eigenmode based model deterministically contains a combination of only those

24 A. Stavrev et. al.

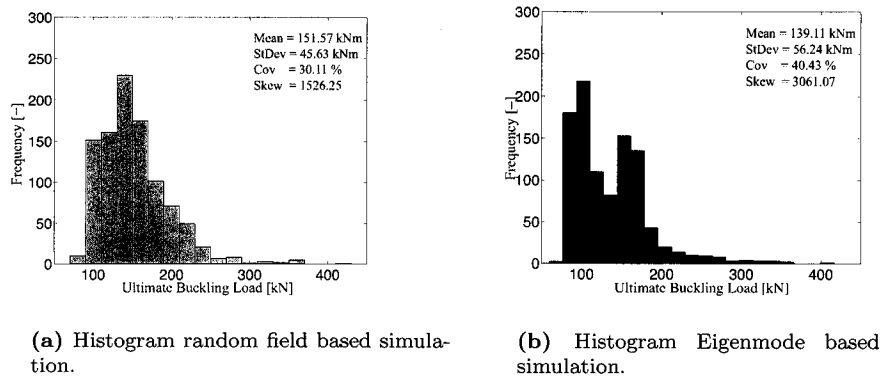


Figure 20: Buckling loads distributions of I-section members for the load case  $M/P = 0.500$ .

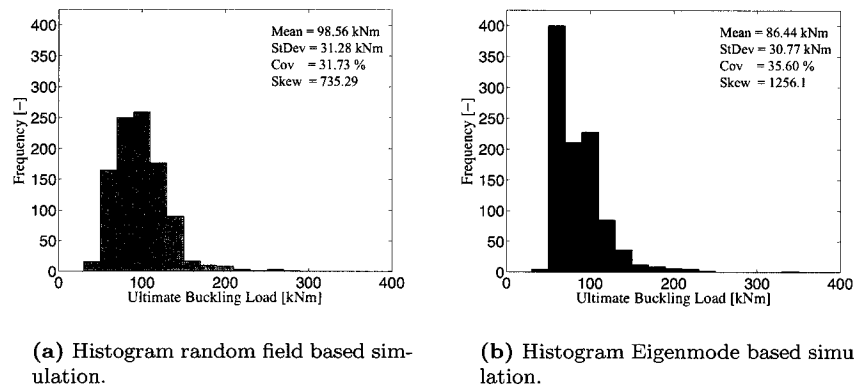


Figure 21: Buckling loads distributions of I-section members for the load case pure major axis bending moment  $M$ .

imperfection modes, which the I-section beam column under consideration can be expected to be most sensitive to.

#### 5.4. The stochastic interaction curve

The influence of combined loading on the ultimate strength of I-section members is typically illustrated by interaction curves<sup>12,16,44</sup> that show corresponding pairs of ultimate axial load and ultimate end moments for different load combinations. Following SCHILLINGER et al.<sup>36</sup>, stochastic interaction curves are derived with both geometric imperfection models for the present I-section beam-column by considering

pure major axis bending  $M$ , pure axial compression  $P$  as well as the four constant combinations  $M/P = 0.050, 0.125, 0.250$  and  $0.500$  m, and are plotted in Figs. 22. and 23. The additional stochastic information of the histograms is incorporated

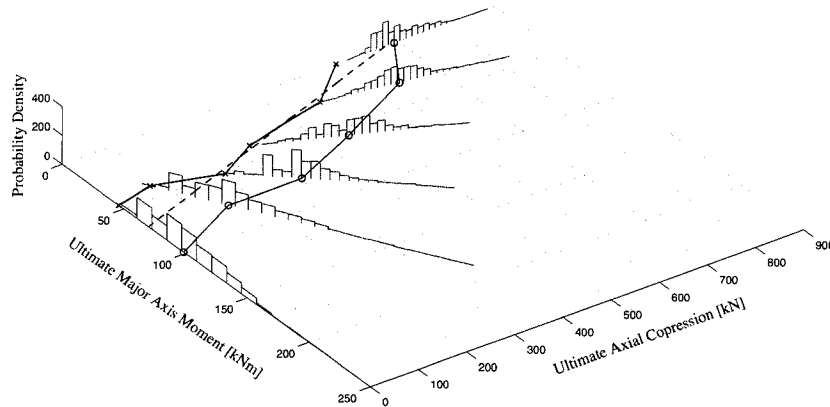


**Figure 22:** Normal force - moment interaction curves for the random field based simulation.

by adding a frequency dimension. Figure 24 compares the curves composed of the means and the lowest buckling loads for each load case and imperfection model with the experimental buckling tests and the interaction formula according to Eurocode 3<sup>46</sup>. The simulated curves have both a convex shape, which is reasonable with respect to similar results in the literature in<sup>16</sup>. The EC3 curve, which has been derived on the basis of large scale experiments<sup>15,44</sup>, can be seen to be optimistic for pure compression, but becomes increasingly conservative with larger bending components. Thus, the EC3 curve reacts to the increase in uncertainty for bending dominated load cases, which is also predicted by simulations in the form of a dramatic increase in the coefficients if variation.

## 6. Summary and conclusions

The present paper compares two stochastic modeling methods for geometric imperfections in their ability to represent the variation of buckling loads of a long I-section beams. In particular, both methods are applied in a similar way starting with the complicated random field approach and calibrating homogeneous and evolutionary power spectra for the local and global imperfections of the beam based on

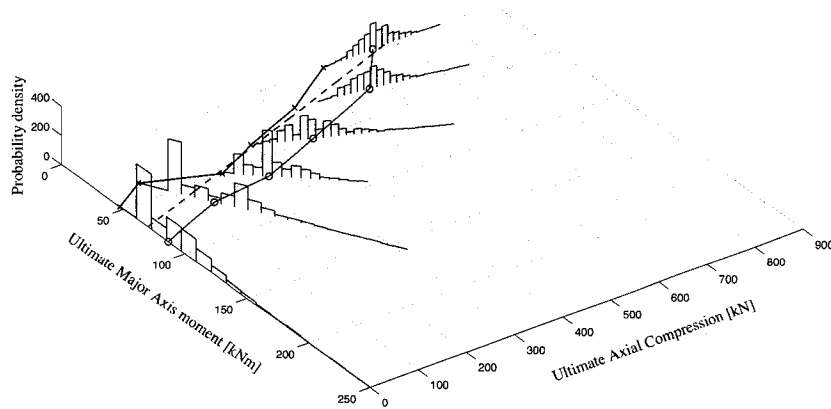


Figure 23: Normal force - moment interaction curves for the random field based simulation.

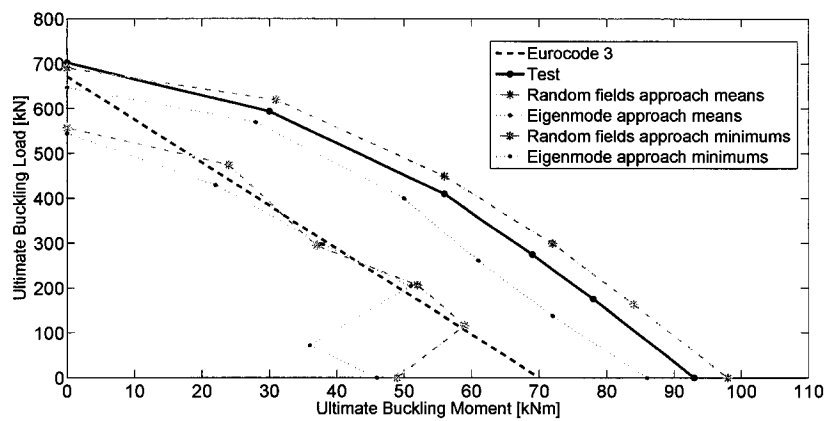


Figure 24: Normal force - moment interaction curves for the random field based simulation.

experimental measurements. Then the same is done for the stochastic eigenmode method by replacing the stochastic theory estimations with conservative assumptions on the safe side and introducing random variables calibrated out of the power spectra from the first approach. Both imperfection models are then discretized with non-linear shell elements using the commercial finite element program "MSC NAS-

28 A. Stavrev et. al.

12. Galambos T (1998) Guide to stability design criteria for metal structures. Wiley, New York.
13. Godoy LA (1999) Theory of elastic stability: analysis and sensitivity, Taylor and Francis, London.
14. Greiner R, Kettler M, Lechner A, Freytag B, Linder J, Jaspart J-P, Boissonnade N, Bortolotti E, Weynand K, Ziller C, Oerder R (2008) Plastic member capacity of semi-compact steel sections - a more Economic Design, Final Report, European Research Fund for Coal and Steel.
15. A.S. Hasham and K.J.R. Rasmussen, Member capacity of thin-walled I-sections in combined compression and major axis bending, *Research Report No R746*, (School of Civil Engineering, University of Sydney, 1997).
16. A.S. Hasham and K.J.R. Rasmussen, Non-linear analysis of locally buckled I-section steel beam-columns. In: Zaras J, Kowal-Michalska K, Rhodes J (eds) *Thin-walled structures-advances and developments*. Proc. 3rd Int. Conf. on thin-walled structures. Elsevier, Krakow, pp 427-436.
17. A.S. Hasham and K.J.R. Rasmussen, Interaction curves for locally buckled I-section beam-columns. *J Constr Steel Res* 58:213-241 (2002).
18. Kala Z (2005) Sensitivity analysis of the stability problems of thin-walled structures. *J Constr Steel Res* 61(3):415-422.
19. Kolanek K, Jendo S (2008) Random field models of geometrically imperfect structures with clamped boundary conditions. *Probab Eng Mech* 23(2):219-226.
20. Newland D.E., *An introduction to random vibrations, spectral and wavelet analysis*. Wiley, New York 1993.
21. Papadopoulos V, Papadrakakis M, Finite element analysis of cylindrical panels with random initial imperfections. *J Eng Mech* 130:867-876 (2004).
22. Papadopoulos V, Papadrakakis M, The effect of material and thickness variability on the buckling load of shells with random initial imperfections. *Comput Methods App Mech Eng* 194:1405-1426 (2005).
23. Papadopoulos V, Iglisis P, The effect of non-uniformity of axial loading on the buckling behavior of shells with random imperfections. *Int J Solids Struct* 44:6299-6317 (2007).
24. Papadopoulos V, Charnpits DC, Papadrakakis M, A computationally efficient method for the buckling analysis of shells with stochastic imperfections. *Comput Mech* 43: 687-700 (2008).
25. Papadopoulos V, Stefanou G, Papadrakakis M, Buckling analysis of imperfect shells with stochastic non-Gaussian material and thickness properties. *Int J Solids Struct* 46:2800-2808 (2009).
26. Papoulis A, Pillai SU, *Probability, random variables and stochastic processes*. McGraw-Hill, New York (2002).
27. Priestley MB, *Spectral analysis and time series*. Academic Press, London (1991).
28. Priestley MB, *Nonlinear and non-stationary time series analysis*, Academic Press, London (1998).
29. Ramm E, Wall W, Shell structures. A sensitive interrelation between physics and numerics. *Int J Numer Methods Eng* 60:381-427 (2004).
30. Rasmussen KJR, Hancock GJ, Buckling analysis of thin-walled structures: numerical developments and applications. *Prog Struct Eng Mater* 2(3):359-368 (2000).
31. Schafer BW, Grigoriu M, Pekoez T, A probabilistic examination of the ultimate strength of cold-formed steel elements. *Thin Walled Struct* 31:271-288 (1988).
32. Schenk CA, Schueller GI, Buckling analysis of cylindrical shells with random geometric imperfections. *Int J Non Linear Mech* 38:1119-1132 (2003).

TRAN” and the stochastic buckling behaviour of the I-section beam is examined with two identical, large scale Monte-Carlo simulations. The ability of both methods to represent the vast variation of the buckling loads for different load cases, depending exclusively on geometric imperfections is confirmed by comparison to real-life buckling tests. With respect to load-displacement response, failure modes and key stochastic parameters both methods are in a comprehensible agreement with each other and experiments. It is outlined, that both methods offer a deeper insight in the buckling behaviour of I-section beam-columns and are well suited for praxis applications like extending expensive and time-consuming real-life buckling tests with large scale numerical simulations. Furthermore the eigenmode approach is a very simply and simultaneously accurate enough alternative to the precise random field method, allowing further exploitation of fast and reliable stochastic computations in order to provide better understanding of the physical behaviour of thin-walled structures.

### **Acknowledgments**

This section should come before the References and should be unnumbered. Funding information may also be included here.

### **References**

#### **Bibliography**

1. Argyris J, Papadrakakis M, Stefanou G (2002) Stochastic finite element analysis of shells. *Comput Methods Appl Mech Eng* 191:4781-4804.
2. Basudhar A, Missoum S (2009) A sampling-based approach for probabilistic design with random fields. *Comput Methods Appl Mech Eng*, 189(33):3647-3655.
3. Blyfield MP, Nethercot DA (1997) Material and geometric properties of structural steel for use in design. *Struct Eng* 75(21):1-5.
4. Budiansky B (1974) Theory of buckling and post-buckling behavior of elastic structures. *Advances in applied mechanics*, vol 14 Academic Press, New York, pp 1-65.
5. Bushnell D (1985) *Computerized buckling analysis of shells*. Springer, New York.
6. Bazant ZP, Cedolin L (1991) *Stability of structures: elastic, inelastic, fracture and damage theories*. Kluwer, Dordrecht.
7. Chen N-Z, Guedes Soares C (2008) Spectral stochastic finite element analysis for laminated composite plates. *Comput Methods Appl Mech Eng* 197:4830-4839.
8. Craig KJ, Roux WJ (2008) On the investigation of shell buckling due to random geometrical imperfections implemented using Karhunen-Loeve expansions. *Int J Numer Methods Eng* 73:1715-1726.
9. Crisfield MA (1997) *Non-linear finite element analysis of solids and structures*, vol 1+2. Wiley, New York.
10. Deodatis G, Spanos PD (eds) (2006) *Computational stochastic mechanics*. In: *Proceedings of the 5th International conference on computational stochastic mechanics (CSM-5)*, IOS Press, Amsterdam.
11. Elishakoff I (2000) Uncertain buckling: its past, present and future. *Int J Solids Struct* 37: 6869-6889.

33. Schenk CA, Schueller GI, Uncertainty assesment of large finite elements systems, Lecture Notes in applied and computational mechanics, vol. 24, Springer, Berlin (2005).
34. Schenk Ca, Schueller GI, Buckling analysis of cylindrical shells with cutouts including random boundary and geometric imperfections. *Comput Methods Appl Mech Eng* 196:3424-3434 (2007).
35. D. Schillinger, V. Papadopoulos M. Bischoff, M. Papadrakakis, Buckling analysis of imperfect I-section beam-columns with stochastic shell finite elements, in *Comput. Mech.* (2010) 46:495-510.
36. D. Schillinger and V. Papadopoulos, Buckling analysis of imperfect I-Section beam-columns with stochastic shell finite elements, in *Comp. Methods Appl. Mech. Engrg.* 46 (2010) 495-510.
37. Shinozuka M, Deodatis G, Simulation of stochastic processes by spectral representation. *App Mech Rev (ASME)* 44:191-203 (1991).
38. Shinozuka M, Deodatis G, Simulation of multi-dimensional Gaussian stochastic fields by spectral representation. *Appl Mech Rev (ASME)* 49:29-53 (1996).
39. Stefanou G, Papadrakakis M, Stochastic finite element analysis of shells with combined random material and geometric properties. *Comput Methods Appl Mech Eng* 193:139-160. (2004).
40. Stefanou G, Papadrakakis M, Assesment of spectral representation and Karhunen-Loeve expansion methods for the simulation of Gaussian stochastic fields. *Comput Methods Appl Mech Eng* 196:2465-2477 (2007).
41. Stefanou G, The stochastic finite element method: past, present and future. *Comput Methods Appl Mech Eng* 198:1031-1051 (2009).
42. Sudret B, Der Kiureghian A, Stochastic finite element methods and reliability: a state-of-art report, Rep. No. UCB/SEMM-2000/08, University of California at Berkley, USA (2000).
43. Tootkaboni M, Graham-Brady L, Schafer BW, Geometrically non-linear behavior of structural systems with random material property: an asymptotic spectral stochastic approach. *Comput Methods Appl Mech Eng* 198:3173-3185 (2009).
44. Trahair NS, Bradford MA, Nethercot DA, Gardner L, The behaviour and design of steel structures to EC3, Taylor and Francis, London. (2008).
45. Vanmarcke E, Random fields analysis and synthesis. The MIT Press, MA, Cambridge. (1983).
46. *Eurocode 3: Design of steel structures, DIN EN 1993-1-1:2005*, (DIN 2007).